J|A|C|S
ARTICLES
Published on Web 02/05/2004

Calculating the Electron Paramagnetic Resonance Parameters of Exchange Coupled Transition Metal Complexes Using Broken Symmetry Density Functional Theory: Application to a Mn^{III}/Mn^{IV} Model Compound

Sebastian Sinnecker,[†] Frank Neese,*[,†] Louis Noodleman,[‡] and Wolfgang Lubitz*[,†]

Contribution from the Max-Planck-Institut für Bioanorganische Chemie, Stiftstr. 34-36, D-45470 Mülheim an der Ruhr, Germany, and Department of Molecular Biology, TPC 15, The Scripps Research Institute, La Jolla, California 92037

Received October 13, 2003; E-mail: Lubitz@mpi-muelheim.mpg.de; Neese@mpi-muelheim.mpg.de

Abstract: The capability of the density functional broken symmetry approach for the calculation of various EPR parameters of exchange coupled metal clusters is demonstrated by studying the experimentally well-investigated $[Mn^{III}Mn^{IV}(\mu\text{-}O)_2(\mu\text{-}OAc)DTNE]^{2+}$ complex. Geometry optimizations of the complex in its broken symmetry and high spin states yielded structures with two distinct manganese sites and geometrical parameters in good agreement with the X-ray structure. Exchange coupling constants were calculated from the energy differences between the high spin and broken symmetry states using the Heisenberg spin Hamiltonian. Very good agreement between theory and experiment was achieved with the B3LYP hybrid functional. The *g*-tensor calculations were performed employing the coupled perturbed Kohn−Sham equations. A strategy for the computation of *g*-tensor site values is presented and provides single-site *g*-tensors that are in good agreement with the expectations for Mn^{III} and Mn^{IV}, respectively. Spin projection gave the *g*-tensor of the coupled manganese complex in very good agreement with the experimental results. Complete ^{55}Mn hyperfine tensors, including spin−orbit contributions, were calculated and spin-projected. The source of anisotropy in this system could be traced back to the Mn^{III} ion in line with the experimental results. The isotropic manganese hyperfine coupling constants were underestimated by factors between 1.4 and 2.5. It is shown that this deficiency is systematic in character and not anchored in the broken symmetry approach. Nuclear quadrupole splitting of the ^{55}Mn nuclei is shown to be small in this system. In addition, ^{14}N and ^{1}H ligand hyperfine data were calculated and compared well with the experimental results. The quality of the extended point-dipole model was demonstrated in application to ^{1}H anisotropic hyperfine coupling constants.

1. Introduction

Exchange coupled metal clusters play an important role in biochemistry, where they provide the functional basis of many native redox systems such as copper, manganese, or iron proteins.[1] Over the last years, an increasing number of model systems of redox protein cofactors has been studied theoretically. This includes work on iron sulfur clusters,[2−6] the manganese catalase active site,[7−9] nitrogenases,[5,10,11] and the cofactor of methane monooxygenase.[12−14] Likewise, computational investigations of the water oxidizing tetranuclear manganese clusters of photosystem II are available.[15,16] The main focus of these studies was the calculation of geometrical parameters, reaction pathways, Heisenberg exchange coupling constants, and ^{57}Fe-Mössbauer data. While there is substantial progress in the calculation of spectroscopic properties of metalloproteins in general,[17] there were only a few attempts for the calculation of electron paramagnetic resonance (EPR) or electron−nuclear double resonance (ENDOR) parameters of exchange coupled metal clusters.[2] This situation is especially promising for theoretical work due to the rich EPR and ENDOR spectra of

[†] Max-Planck-Institut für Bioanorganische Chemie.
[‡] The Scripps Research Institute.

(1) Bencini, A.; Gatteschi, D. *EPR of Exchange Coupled Systems*; Springer-Verlag: Berlin, 1990.
(2) Mouesca, J. M.; Noodleman, L.; Case, D. A.; Lamotte, B. *Inorg. Chem.* **1995**, *34*, 4347−4359.
(3) Noodleman, L.; Chen, J. L.; Case, D. A.; Giori, C.; Rius, G.; Mouesca, J. M.; Lamotte, B. In *Nuclear Magnetic Resonance of Paramagnetic Macromolecules*; La Mar, G. N., Ed.; Kluwer Academic Publishers: Leiden, The Netherlands, 1995; pp 339−367.
(4) Noodleman, L. *Inorg. Chem.* **1988**, *27*, 3677−3679.
(5) Noodleman, L.; Lovell, T.; Liu, T. Q.; Himo, F.; Torres, R. A. *Curr. Opin. Chem. Biol.* **2002**, *6*, 259−273.
(6) Li, J.; Noodleman, L.; Case, D. A. In *Inorganic Electronic Structure and Spectroscopy*; Solomon, E. I., Lever, A. B. P., Eds.; John Wiley and Sons: New York, 1999; Vol. 1, pp 661−724.
(7) Siegbahn, P. E. M. *J. Comput. Chem.* **2001**, *22*, 1634−1645.
(8) Siegbahn, P. E. M. *Theor. Chem. Acc.* **2001**, *105*, 197−206.
(9) Siegbahn, P. E. M. *Curr. Opin. Chem. Biol.* **2002**, *6*, 227−235.
(10) Lovell, T.; Li, J.; Liu, T. Q.; Case, D. A.; Noodleman, L. *J. Am. Chem. Soc.* **2001**, *123*, 12392−12410.
(11) Lovell, T.; Li, J.; Case, D. A.; Noodleman, L. *J. Am. Chem. Soc.* **2002**, *124*, 4546−4547.
(12) Lovell, T.; Han, W. G.; Liu, T. Q.; Noodleman, L. *J. Am. Chem. Soc.* **2002**, *124*, 5890−5894.
(13) Lovell, T.; Li, J.; Noodleman, L. *Inorg. Chem.* **2001**, *40*, 5251−5266.
(14) Lovell, T.; Li, J.; Noodleman, L. *Inorg. Chem.* **2001**, *40*, 5267−5278.
(15) Schmitt, E. A.; Noodleman, L.; Baerends, E. J.; Hendrickson, D. N. *J. Am. Chem. Soc.* **1992**, *114*, 6109−6119.
(16) Siegbahn, P. E. M. *Inorg. Chem.* **2000**, *39*, 2923−2935.
(17) Neese, F. *Curr. Opin. Chem. Biol.* **2003**, *7*, 125−135.

these species. In this context, exchange coupled manganese enzyme active sites are ideal systems.[18,19] EPR methods are well-suited for the investigation of redox protein active sites since they are only sensitive to open shell systems such as metal cofactors, while the rest of the (diamagnetic) protein backbone is EPR silent. The geometric and electronic structure information available from EPR and ENDOR experiments on open-shell systems is condensed in the *g*-tensor, hyperfine coupling constants (hfc's), and nuclear quadrupole coupling constants (nqc's). These properties describe the full interaction between the radical and the magnetic field, between the unpaired electrons and magnetic nuclei, and between nonspherical nuclear charge distributions and electric field gradients, respectively.

Exchange coupled metal clusters are characterized by weak interactions between two magnetic metal centers with unpaired electrons. In these systems, the individual spins of the metal sites are coupled to a number of energetically close lying electronic levels.[1,20] A direct approach to the theoretical description of such a coupled spin system requires multideterminant-based methods.[21−24] They are limited, however, to rather small molecules due to the high computational effort involved, i.e., active sites of protein systems are usually out of reach. A way out of this dilemma is the use of the broken symmetry density functional method (BS-DFT).[25−30] In this approach, the real multideterminant electronic state with unpaired α- and *β*-electrons involving both metal centers is described by a single-determinant Kohn−Sham wave function with unpaired α- and *β*-electrons partially localized at different metal sites.[29] The energies, spin expectation values, and spin densities of the bs (broken symmetry) state differ from those of the multideterminant antiferromagnetic state, but its exchange coupling constants, hyperfine coupling constants, and *g*-tensor can be obtained from "mapping procedures" using spin Hamiltonians and spin projection methods.[1,31] The BS-DFT approach can provide reasonable geometries, energies, and exchange coupling constants, as has been shown in many studies. The calculation of *g*- and hyperfine tensors is, however, rather limited and was done, for example, for 2-Fe ferredoxin model systems.[32]

Ultimately, our goal is to combine theory and experiment to elucidate the geometric and electronic structures of oligonuclear manganese complexes in proteins. These sites are often inaccessible to X-ray crystallography, because either they are short-lived (in the case of intermediates) or the protein is difficult to crystallize. In these cases, spectroscopy must be relied on as the only source of structural information. However, to develop the information content of the spectra to its full potential, an as detailed as possible interpretation of the spectroscopic parameters is necessary. It is this area where the theoretical methods have their highest potential. However, prior to any application, it is essential to rigorously assess the reliability of a given theoretical procedure. Since there are very few theoretical EPR spectroscopic studies on exchange coupled dimers, we have decided to focus first on the experimentally well-investigated synthetic, mixed valence dinuclear manganese complex $[Mn^{III}Mn^{IV}(\mu\text{-}O)_2(\mu\text{-}OAc)DTNE]^{2+}$ (Figure 1, complex **1**). This species and related dinuclear manganese complexes have been experimentally investigated as a basis for obtaining a deeper understanding of the manganese catalase and the oxygen-evolving complex of photosystem II.[33,34] A few similar clusters were already the subjects of quantum chemical studies. Delfs and Stranger investigated the influence of the bridging oxo-ligands and the metal oxidation states on the magnetic coupling in dimeric manganese complexes, but with the simplification that ammonia was used as the terminal ligands.[35−37] A similar theoretical study on dinuclear manganese complexes was performed employing the more rigid, tridentate TACN (1,4,7-triazacyclononane) ligands.[38] Other theoretical data can be found for the $[Mn^{III}Mn^{III}(\mu\text{-}O)(\mu\text{-}OAc)_2(CH_3)_3TACN)_2]^{2+}$ complex in a study combining optical spectroscopy with BS-DFT.[39]

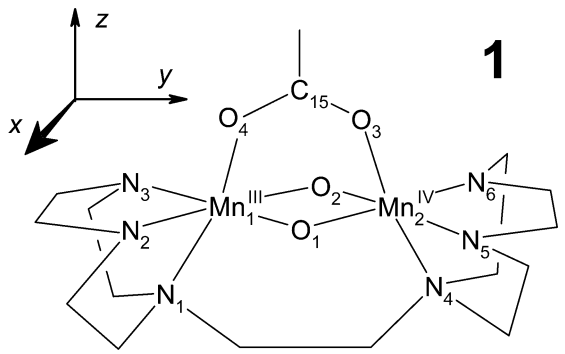

Figure 1. Structure, numbering, and the molecular coordinate system of the $[Mn^{III}Mn^{IV}(\mu\text{-}O)_2(\mu\text{-}OAc)DTNE]^{2+}$ complex **1**. DTNE = 1,2-bis(1,4,7-triazacyclonon-1-yl)ethane).

In this work, the suitability of different density functionals and basis sets for the calculation of EPR parameters from BS-DFT is tested in application to the dinuclear manganese complex **1**. Results from geometry optimization are reported together with Heisenberg exchange coupling constants. Furthermore, and to the best of our knowledge, theoretical hyperfine and nuclear quadrupole tensors as well as molecular *g*-tensors are given for the first time for such a Mn^{III}/Mn^{IV} complex.

2. Methodological Details

Complex **1** is characterized by two magnetic metal centers with site spins of $S_1 = 2$ for Mn^{III} and $S_2 = 3/2$ for Mn^{IV}. Parallel and antiparallel

(18) Wieghardt, K. *Angew. Chem., Int. Ed. Engl.* **1989**, *28*, 1153−1172.
(19) Dismukes, G. C. *Chem. Rev.* **1996**, *96*, 2909−2926.
(20) Kahn, O. *Molecular Magnetism*; VCH Publishers: Weinheim, Germany, 1993.
(21) Kolczewski, C.; Fink, K.; Staemmler, V. *Int. J. Quantum. Chem.* **2000**, *76*, 137−147.
(22) Fink, K.; Wang, C.; Staemmler, V. *Inorg. Chem.* **1999**, *38*, 3847−3856.
(23) Calzado, C. J.; Cabrero, J.; Malrieu, J. P.; Caballol, R. *J. Chem. Phys.* **2002**, *116*, 3985−4000.
(24) Calzado, C. J.; Cabrero, J.; Malrieu, J. P.; Caballol, R. *J. Chem. Phys.* **2002**, *116*, 2728−2747.
(25) Illas, F.; Moreira, I. D. R.; de Graaf, C.; Barone, V. *Theor. Chem. Acc.* **2000**, *104*, 265−272.
(26) Koch, W.; Holthausen, M. C. *A Chemist's Guide to Density Functional Theory*; Wiley-VCH: Weinheim, Germany, 2000.
(27) Hohenberg, P.; Kohn, W. *Phys. Rev. B* **1964**, *136*, 864.
(28) Kohn, W.; Sham, L. J. *Phys. Rev.* **1965**, *140*, 1133.
(29) Noodleman, L.; Davidson, E. R. *Chem. Phys.* **1986**, *109*, 131−143.
(30) Noodleman, L. *J. Chem. Phys.* **1981**, *74*, 5737−5743.
(31) Zheng, M.; Khangulov, S. V.; Dismukes, G. C.; Barynin, V. V. *Inorg. Chem.* **1994**, *33*, 382−387.
(32) Noodleman, L.; Baerends, E. J. *J. Am. Chem. Soc.* **1984**, *106*, 2316−2327.
(33) Schäfer, K. O.; Bittl, R.; Zweygart, W.; Lendzian, F.; Haselhorst, G.; Weyhermüller, T.; Wieghardt, K.; Lubitz, W. *J. Am. Chem. Soc.* **1998**, *120*, 13104−13120.
(34) Schäfer, K. O.; Bittl, R.; Lendzian, F.; Barynin, V.; Weyhermüller, T.; Wieghardt, K.; Lubitz, W. *J. Phys. Chem. B* **2003**, *107*, 1242−1250.
(35) Delfs, C. D.; Stranger, R. *Inorg. Chem.* **2000**, *39*, 491−495.
(36) Delfs, C. D.; Stranger, R. *Inorg. Chem.* **2001**, *40*, 3061−3076.
(37) McGrady, J. E.; Stranger, R. *J. Am. Chem. Soc.* **1997**, *119*, 8512−8522.
(38) Zhao, X. G.; Richardson, W. H.; Chen, J. L.; Li, J.; Noodleman, L.; Tsai, H. L.; Hendrickson, D. N. *Inorg. Chem.* **1997**, *36*, 1198−1217.
(39) Brunold, T. C.; Gamelin, D. R.; Solomon, E. I. *J. Am. Chem. Soc.* **2000**, *122*, 8511−8523.

Scheme 1[a]

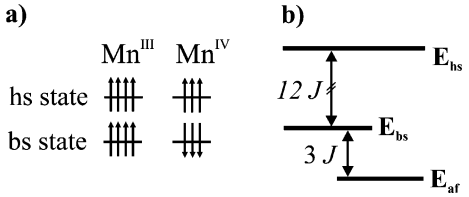

(a) Formal "site spin" orientations in the high spin (hs) and broken symmetry (bs) states of a Mn^{III}/Mn^{IV} complex. (b) The Heisenberg exchange coupling constant J can be used for estimating the energy separation between the hs, bs, and the real antiferromagnetic (af) states.

coupling of the individual spins yields effective spins of $M_S = 7/2$ for the high spin (hs) state and $M_S = 1/2$ for the broken symmetry (bs) state (Scheme 1). The energetical arrangement of the spin states is determined by the Heisenberg exchange coupling constant J. Employing the standard definition for the spin-Hamiltonian

$$H = -2JS_1S_2, \tag{1}$$

J can be calculated from the energy differences between high spin and broken symmetry states:[40]

$$J = -\frac{E_{hs} - E_{bs}}{4S_1S_2} \tag{2}$$

J determines the energies of the entire spin state ladder by

$$E(S) = -JS(S+1) \tag{3}$$

and can be used for determining the energy separations between the electronic states of interest (see Scheme 1). Equation 2 is valid only for the weak interaction limit and is equivalent to the expressions used in other studies on mixed valence systems.[32,36] Alternatively, J can be evaluated from Yamaguchi's expression by[41,42]

$$J = -\frac{E_{hs} - E_{bs}}{\langle S_{hs}^2\rangle - \langle S_{bs}^2\rangle} \tag{4}$$

as it was shown previously.[43] Note that the Heisenberg spin-Hamiltonian implies that the spatial part of the wave functions remains identical for all spin multiplets. Furthermore, resonance delocalization was not taken into account in this work due to the trapped valence character of complex **1**.[33]

The electron density of the bs state should correspond very well to the electron density of the real antiferromagnetic state.[26] In consequence, electric field gradients and nuclear quadrupole coupling constants calculated for the bs state can be directly compared to experimental results obtained for the antiferromagnetic state. In contrast, the calculated spin densities of the bs state differ considerably from those of the antiferromagnetic state. Therefore, the computed hyperfine data and g-tensors have to be corrected by spin projection.[33,44]

In this paper, we will use the approximation of strong exchange coupling and construct the total (observable) magnetic interaction tensors from fictitious local single-site tensors using straightforward spin coupling algebra.[1,31,33] The problem is thus reduced to computing these local site tensors from DFT calculations on the high spin and broken symmetry states, respectively. The two spin sites $i = 1, 2$ of the dinuclear metal complex are treated as isolated spin systems with g-tensor site values g_i and ^{55}Mn hyperfine site values $A_1(Mn^{III})$ and $A_2(Mn^{IV})$. These site values should be comparable to spectroscopic parameters of similar mononuclear systems. Furthermore, each magnetic ligand nucleus n (e.g., ^{14}N or ^{1}H) can be assigned to one of the spin sites i and is described likewise by a hyperfine site value $A_i(n)$. The criterion for assigning a nucleus to either the Mn^{III} or the Mn^{IV} site is based on the distance to the respective Mn center. Such an assignment is safe for the nitrogen atoms and the neighboring hydrogen nuclei of complex **1** (Figure 1). However, bridging ligands cannot be treated based on this criterion. Vector coupling of the two magnetic sites leads to the following equations for the calculation of the effective g-tensor and the nuclear hyperfine coupling constants (also tensors) of the exchange coupled complex:[33]

$$\mathbf{g} = c_1\mathbf{g}_1 + c_2\mathbf{g}_2 + \frac{c_1c_2}{5J}(\mathbf{g}_1 - \mathbf{g}_2)[(3c_1+1)\cdot\mathbf{d}_1 - (3c_2+1)\cdot\mathbf{d}_2] \tag{5}$$

$$\mathbf{A_1} = c_1\mathbf{a_1} - \frac{\mathbf{a_1}}{5J}c_1c_2[(3c_1+1)\cdot\mathbf{d_1} - (3c_2+1)\cdot\mathbf{d_2}] \tag{6}$$

$$\mathbf{A}_2 = c_2\mathbf{a}_2 + \frac{\mathbf{a_2}}{5J}c_1c_2[(3c_1+1)\cdot\mathbf{d_1} - (3c_2+1)\cdot\mathbf{d_2}] \tag{7}$$

For the present system, spin projection coefficients $c_1 = 2$ and $c_2 = -1$ result from the spin coupling model for the Mn^{III} and Mn^{IV} sites, respectively.[33] However, the additional zero-field splitting contributions (d_i) arising in eqs 5−7 can be neglected in first order for this Mn^{III}/Mn^{IV} complex due to the large J-value (>100 cm^{-1}) that dominates over the relatively small zero-field splitting of the manganese ions (d_i < 5 cm^{-1}).[31,33] In consequence, the equations for the spin projection can be simplified to

$$\mathbf{g} = c_1\mathbf{g}_1 + c_2\mathbf{g}_2 \tag{8}$$

$$\mathbf{A_1} = c_1\mathbf{a_1} \tag{9}$$

$$\mathbf{A}_2 = c_2\mathbf{a}_2 \tag{10}$$

The additional error introduced by this approximation is certainly ≤10%.

In contrast to the hfc's, the g-tensor is an integral property of the dinuclear complex. Thus, g-tensor site values must be obtained prior to the spin projection of eq 8. In this work, the g-tensor site values are extracted from the calculated effective g-tensors of both, the hs and bs states: The hs g-tensor can be decomposed into contributions C_1 and C_2 from sites 1 and 2. Neglecting electronic relaxation, the hs and bs states differ only by a spin flip of all magnetic electrons on site 2; see, for example, eq 17. Therefore, one can assume that the g-tensor of the bs state is made up from the same contributions C_1 and C_2, differing only in the sign of C_2 due to the rotation of the spin vector on that site:

$$\mathbf{g_{hs}} = \frac{1}{S_{hs}}(C_1 + C_2) \tag{11}$$

and

$$\mathbf{g_{bs}} = \frac{1}{S_{bs}}(C_1 - C_2) \tag{12}$$

Defining g-tensor site values:

$$\mathbf{g_1} = \frac{1}{S_1}C_1 \tag{13}$$

and

$$\mathbf{g_2} = \frac{1}{S_2}C_2 \tag{14}$$

(40) Mouesca, J. M.; Chen, J. L.; Noodleman, L.; Bashford, D.; Case, D. A. *J. Am. Chem. Soc.* **1994**, *116*, 11898−11914.
(41) Soda, T.; Kitagawa, Y.; Onishi, T.; Takano, Y.; Shigeta, Y.; Nagao, H.; Yoshioka, Y.; Yamaguchi, K. *Chem. Phys. Lett.* **2000**, *319*, 223−230.
(42) Yamaguchi, K.; Takahara, Y.; Fueno, T. In *Applied Quantum Chemistry*; Smith, V. H., Schaefer, F., Morokuma, K., Eds.; Reidel: Dordrecht, The Netherlands, 1986; p 155.
(43) Ghosh, P.; Bill, E.; Weyhermüller, T.; Neese, F.; Wieghardt, K. *J. Am. Chem. Soc.* **2003**, *125*, 1293−1308.
(44) Sands, R. H.; Dunham, W. R. *Q. Rev. Biophys.* **1974**, *7*, 443−504.

and inserting these equations in eqs 11 and 12, we obtain the following expressions for the calculation of the *g*-tensor site values ($M_S^{hs} = S_1 + S_2$ and $M_S^{bs} = |S_1 - S_2|$):

$$\mathbf{g_1} = \frac{1}{2S_1}[g_{hs}M_S^{hs} + g_{bs}M_S^{bs}] \quad (15)$$

$$\mathbf{g_2} = \frac{1}{2S_2}[g_{hs}M_S^{hs} - g_{bs}M_S^{bs}] \quad (16)$$

3. Computational Details

Geometry Optimization. Geometry optimizations of complex **1** in the hs and bs states were performed to study the influence of different density functionals,[26] the basis sets, and the frozen core approximation on the geometrical parameters. For that purpose, two different quantum chemical programs were used: ADF 2000.02[45,46] and ORCA 2.2.[47] Both programs offer pure density functional methods such as the BP functional,[48−50] while hybrid density functionals such as B3LYP are only available in ORCA.[51−53] In contrast, the frozen core approximation is available only in ADF. The ADF calculations were performed with the triple-ζ Slater type basis set IV for manganese and the double-ζ basis sets III for all other elements from the ADF library, respectively. The ORCA calculations were performed employing Gaussian-type basis sets: TZVPP[54] for Mn and DZP[55] for all other elements from the Turbomole 5.3 library, respectively.[56] Altogether, five geometry optimizations were performed:

(1) ADF-1: BP functional. Basis sets IV (Mn), III (other elements). 1s frozen core for C, N, and O.

(2) ADF-2: BP functional. Basis sets IV (Mn), III (other elements). 1s−3p frozen core for Mn, 1s for C, N, and O.

(3) ADF-3: BP functional. Basis sets IV (Mn), III (other elements). All-electron calculation.

(4) ORCA-1: BP functional. Basis sets TZVPP (Mn), DZP (other elements). All-electron calculation.

(5) ORCA-2: B3LYP functional. Basis sets TZVPP (Mn), DZP (other elements). All-electron calculation.

Both ORCA calculations were speeded up using the RI approximation.[57−59] For that purpose, the TZV/J (Mn) and SV/J (H, C, N, and O) auxiliary basis sets[58,60] from the Turbomole 5.3 basis set library were used.[61]

Refined Single-Point Calculations. Hyperfine coupling constants, nuclear quadrupole coupling constants, and *g*-tensors were obtained from single-point calculations with more accurate methods employing the optimized geometries of complex **1**. The integration accuracy was enhanced to decrease the errors in the spin densities caused by their oscillation with respect to the numerical integration accuracy (ADF: ACCINT = 6 and ORCA: SpecialGridIntAcc = 7 for the Mn nuclei).[62] The basis sets used in the ORCA calculations were replaced with basis functions better adapted for the calculation of core properties: The TZVPP manganese basis set was substituted with the triply polarized (17s11p5d1f) → [17s7p3d1f] core property basis set CP(PPP),[62] the DZP basis functions for H, C, N, and O were replaced with the EPR-II basis sets.[63] In addition, the RI approximation was abandoned to avoid possible artifacts arising from the incompleteness of the auxiliary basis sets. An additional B3LYP single-point calculation was performed with ORCA employing the geometries obtained with the BP functional in ORCA. This was labeled as ORCA-3.

Spectroscopic Parameters. Exchange coupling constants were calculated from the energy differences of the hs and bs states according to eq 2. The exchange pathways are discussed by an analysis of the corresponding orbitals of all magnetic electrons, based on the formalism introduced by Amos and Hall.[64]

The *g*-tensor calculations were only performed with ORCA because the ZORA method[65,66] used in ADF can only be applied to the case of a single unpaired electron. The *g*-shifts Δg from the free electron g_e value of 2.002319 were obtained employing the coupled-perturbed Kohn−Sham equations[67] in conjunction with a parametrized one-electron spin−orbit operator.[68−70] This approach covered spin−orbit coupling, spin-polarization, relativistic mass, and diamagnetic gauge corrections. The *g*-tensor was calculated as a second derivative property of the energy with respect to the external magnetic field and the electron magnetic moment. The dominant cross term contribution between the orbital Zeeman (OZ) and the spin−orbit coupling operators (SOC), $\Delta g^{OZ/SOC}$, is expressed through the first-order wave function coefficients *U* with respect to a magnetic field perturbation:[67]

$$\Delta g_{rs}^{OZ/SOC} = -\frac{1}{\beta S}\sum_{\sigma=\alpha,\beta}(-1)^{\delta_{\sigma\beta}}\sum_{i,a\in\sigma}\mathrm{Im}(U_{ia}^{\sigma;r})\cdot \mathrm{Im}(\langle\psi_i^{\sigma(0)}\left|\sum_A \xi(r_A)\vec{l}_{A,s}\right|\psi_a^{\sigma(0)}\rangle) \quad (17)$$

In this equation, *r* is a component of the magnetic field ($r = x, y, z$) and *s* is a component of the electron spin vector operator ($s = x, y, z$), β denotes the Bohr magneton and *S* is the total spin of the system, $\psi_i^{\sigma(0)}$ describes the occupied zeroth order molecular orbitals with $\sigma = \alpha$, β, and $\psi_a^{\sigma(0)}$ stands for the virtual orbitals, $\vec{l}_{A,s}$ is the angular momentum of the electron relative to nucleus *A*, and $\xi(r_A)$ is the function describing the spin−orbit coupling by effective nuclear charges.[68−70]

The *g*-tensor site values were obtained from the approach discussed in section 2. The molecular *g*-tensors of the antiferromagnetic state were then calculated from spin projection according to eq 8. $\mathbf{g^T g}$ was subsequently diagonalized to yield the final dimer *g*-tensor, i.e., its principal values and orientation.

(45) *ADF* 2000.02; Department of Theoretical Chemistry, Free University of Amsterdam: Amsterdam, The Netherlands, 2000.
(46) Velde, G. T.; Bickelhaupt, F. M.; Baerends, E. J.; Guerra, C. F.; Van Gisbergen, S. J. A.; Snijders, J. G.; Ziegler, T. *J. Comput. Chem.* **2001**, *22*, 931−967.
(47) Neese, F. *ORCA*, version 2.2; an ab initio, density functional, and semiempirical program package; Max-Planck-Institut für Bioanorganische Chemie: Mülheim an der Ruhr, Germany, 2001.
(48) Becke, A. D. *Phys. Rev. A* **1988**, *38*, 3098−3100.
(49) Perdew, J. P. *Phys. Rev. B* **1986**, *34*, 7406.
(50) Perdew, J. P. *Phys. Rev. B* **1986**, *33*, 8822−8824.
(51) Becke, A. D. *J. Chem. Phys.* **1993**, *98*, 5648−5652.
(52) Lee, C. T.; Yang, W. T.; Parr, R. G. *Phys. Rev. B* **1988**, *37*, 785−789.
(53) Stephens, P. J.; Devlin, F. J.; Chabalowski, C. F.; Frisch, M. J. *J. Phys. Chem.* **1994**, *98*, 11623−11627.
(54) Schäfer, A.; Huber, C.; Ahlrichs, R. *J. Chem. Phys.* **1994**, *100*, 5829−5835.
(55) Schäfer, A.; Horn, H.; Ahlrichs, R. *J. Chem. Phys.* **1992**, *97*, 2571−2577.
(56) Ahlrichs, R.; Bär, M.; Baron, H.-P.; Bauernschmitt, R.; Böcker, S.; Ehrig, M.; Eichkorn, K.; Elliot, S.; Furche, F.; Haase, F.; Häser, M.; Horn, H.; Hättig, C.; Huber, C.; Huniar, U.; Kattannek, M.; Köhn, A.; Kölmel, C.; Kollwitz, M.; May, K.; Ochsenfeld, C.; Öhm, H.; Schäfer, A.; Schneider, U.; Treutler, O.; von Arnim, M.; Weigend, F.; Weis, P.; Weiss, H. *Turbomole*, version 5.3; Quantum Chemistry Group, University of Karlsruhe: Karlsruhe, Germany, 2000.
(57) Eichkorn, K.; Treutler, O.; Ohm, H.; Haser, M.; Ahlrichs, R. *Chem. Phys. Lett.* **1995**, *242*, 652−660.
(58) Eichkorn, K.; Weigend, F.; Treutler, O.; Ahlrichs, R. *Theor. Chem. Acc.* **1997**, *97*, 119−124.
(59) Neese, F.; Olbrich, G. *Chem. Phys. Lett.* **2002**, *362*, 170−178.
(60) Eichkorn, K.; Treutler, O.; Ohm, H.; Haser, M.; Ahlrichs, R. *Chem. Phys. Lett.* **1995**, *240*, 283−289.
(61) The basis sets can be downloaded from the ftp server of the Turbomole home page: http://www.turbomole.com.
(62) Neese, F. *Inorg. Chim. Acta* **2002**, *337*, 181−192.
(63) Barone, V. In *Recent Advances in Density Functional Methods*; Chong, D. P., Ed.; World Scientific: Singapore, 1996.
(64) Amos, A. T.; Hall, G. G. *Proc. R. Soc. London* **1961**, *263*, 483−493.
(65) van Lenthe, E.; Wormer, P. E. S.; van der Avoird, A. *J. Chem. Phys.* **1997**, *107*, 2488−2498.
(66) van Lenthe, E.; van der Avoird, A.; Hagen, W. R.; Reijerse, E. J. *J. Phys. Chem. A* **2000**, *104*, 2070−2077.
(67) Neese, F. *J. Chem. Phys.* **2001**, *115*, 11080−11096.
(68) Koseki, S.; Schmidt, M. W.; Gordon, M. S. *J. Phys. Chem.* **1992**, *96*, 10768−10772.
(69) Koseki, S.; Gordon, M. S.; Schmidt, M. W.; Matsunaga, N. *J. Phys. Chem.* **1995**, *99*, 12764−12772.
(70) Koseki, S.; Schmidt, M. W.; Gordon, M. S. *J. Phys. Chem. A* **1998**, *102*, 10430−10435.

^{55}Mn, ^{14}N, and ^{1}H isotropic hyperfine coupling constants a_{iso} and the traceless anisotropic dipolar hfc's a' were calculated directly by both programs from Fermi contact terms and dipolar contributions as the expectation values of the appropriate operators over the spin density. Furthermore, the ^{55}Mn spin−orbit contribution ("orbital" part) of the hyperfine interaction was calculated with ORCA.[71] Its isotropic part (one-third of the trace of the orbital hyperfine tensor) was added to the ^{55}Mn isotropic Fermi contact term a_{iso}, while the anisotropic contribution was added to the anisotropic ^{55}Mn tensor a'. All calculated hyperfine coupling constants $a_{n,iso}$ of the bs state were converted to intrinsic site isotropic hyperfine coupling constants $a_{n,site}$ by

$$a_{n,\mathrm{site}} = \frac{a_{n,\mathrm{iso}} M_S^{bs}}{\pm S_i} \tag{18}$$

S_i is the site spin of the closer manganese center. The positive sign was applied for all atoms on the majority spin site (here: the Mn^{III} center), and the negative sign was applied for those on the minority spin site (Mn^{IV}). The final values A_{iso} that can be compared with the experimental values were then calculated from spin projection according to eqs 9 and 10. The same procedure was applied to the dipolar hyperfine part, yielding the spin projected anisotropic hyperfine coupling constants A'.

The electric field gradients V_{ii}, calculated with the quantum chemical programs, were converted to nuclear quadrupole coupling constants χ by

$$\chi_{ii} = \mathrm{const} \cdot V_{ii} \cdot Q \tag{19}$$

Employing the electric field gradient in atomic units and the nuclear quadrupole moment Q in barn (10^{-28} m^2), we used a factor of const = 234.96 ($=10^{-3} \times e^2/4\pi h\epsilon_0 a_0^3$) for the calculation of χ in MHz. Nuclear quadrupole tensor elements P_{ii} and coupling constants χ_{ii} were related by

$$P_{ii} = \frac{\chi_{ii}}{2I(2I-1)} \tag{20}$$

Here, I is the nuclear spin (^{55}Mn: $I = 5/2$, ^{14}N: $I = 1$). Nuclear quadrupole moments of $Q(^{55}\mathrm{Mn}) = 0.4$ barn and $Q(^{14}\mathrm{N}) = 0.01$ barn were used for the calculation of χ and P.[72]

4. Results and Discussion

4.1. Geometries. All geometry optimizations of the mixed valence complex **1** in its hs and bs states yielded two distinctly different manganese sites in accordance with the X-ray structure (Table 1).[33] Better agreement between theory (hs and bs states) and experiment (af state) was achieved in general for the bs state geometries, but the differences between the geometrical parameters of the high spin and broken symmetry states turned out to be rather small. Similar geometrical parameters were obtained from the BP calculations with ORCA and ADF despite the use of different basis sets. A comparison of the ADF results shows that the frozen core approximation is of minor influence on the geometries. In general, the B3LYP geometry optimization yielded somewhat less accurate geometrical parameters for the bs state than the BP functional.

Mn−Mn distances between 2.55 and 2.62 Å were calculated in our work for complex **1** in its broken symmetry state and were in good agreement with the experimentally determined metal−metal distance of 2.55 Å.[33] A comparable value of 2.59 Å was measured for the closely related complex $[Mn^{III}Mn^{IV}(\mu\text{-}O)_2(\mu\text{-}OAc)TACN_2]^{2+}$ with tetraphenylborate (BPh_4^-) counterions.[73] By contrast, a rather large distance of 2.67 Å was calculated for the $[Mn^{III}Mn^{IV}(\mu\text{-}O)_2(\mu\text{-}OAc)(NH_3)_6]^{2+}$ dication,[36] underlining the influence of rigid multidentate ligands on the metal−metal distance. Other studies have shown that the Mn−Mn distance depends also noticeably on the nature of the metal-bridging ligands and the oxidation states of the manganese atoms.[36,37] It is, however, interesting to note that the Mn−Mn distances are similar to the Fe−Fe distances obtained for comparable ligand sets. For example, a value of 2.63 Å was calculated for an antiferromagnetically coupled dinuclear iron system with an $Fe^{IV}Fe^{IV}(\mu\text{-}O)_2(\mu\text{-}OAc)_2$ core, modeling the intermediate Q of methane monooxygenase.[12]

Table 1. Geometrical Parameters of the bs State of Complex **1**[a]

bond distance	exptl[b]	BP ORCA-1	B3LYP ORCA-2	BP ADF-1	BP ADF-2	BP ADF-3
Mn_1-Mn_2	2.55	2.59 (2.65)	2.62 (2.65)	2.55 (2.64)	2.57 (2.64)	2.56 (2.64)
Mn_1-O_1	1.83	1.83 (1.88)	1.87 (1.88)	1.82 (1.88)	1.83 (1.89)	1.82 (1.88)
Mn_1-O_2	1.83	1.83 (1.89)	1.87 (1.88)	1.82 (1.88)	1.84 (1.89)	1.83 (1.88)
Mn_2-O_1	1.78	1.80 (1.79)	1.77 (1.78)	1.80 (1.79)	1.81 (1.80)	1.80 (1.80)
Mn_2-O_2	1.78	1.80 (1.79)	1.77 (1.77)	1.80 (1.79)	1.80 (1.80)	1.80 (1.79)
Mn_1-N_1	2.21	2.24 (2.31)	2.29 (2.31)	2.27 (2.31)	2.28 (2.32)	2.27 (2.31)
Mn_1-O_4	2.14	2.15 (2.21)	2.20 (2.20)	2.16 (2.21)	2.18 (2.22)	2.16 (2.21)
Mn_2-N_4	2.10	2.11 (2.14)	2.13 (2.13)	2.12 (2.13)	2.14 (2.15)	2.12 (2.13)
Mn_2-O_3	1.97	1.96 (1.94)	1.94 (1.93)	1.95 (1.94)	1.97 (1.95)	1.95 (1.94)
Mn_1-N_2	2.08	2.14 (2.12)	2.13 (2.12)	2.13 (2.11)	2.15 (2.12)	2.13 (2.11)
Mn_1-N_3	2.07	2.15 (2.13)	2.14 (2.13)	2.14 (2.12)	2.16 (2.13)	2.14 (2.12)
Mn_2-N_5	2.08	2.11 (2.13)	2.13 (2.14)	2.10 (2.12)	2.13 (2.14)	2.11 (2.13)
Mn_2-N_6	2.07	2.11 (2.13)	2.13 (2.13)	2.11 (2.12)	2.14 (2.14)	2.11 (2.13)
RMS		0.04 (0.06)	0.05 (0.06)	0.03 (0.05)	0.05 (0.06)	0.04 (0.06)

[a] High spin (hs) state parameters in parenthesis. Comparison with experimental data (antiferromagnetic state). All bond distances in angstroms. Basis sets: TZVPP (Mn) and DZP (other elements) for all ORCA calculations; IV (Mn) and III (other elements) for all ADF calculations. ADF-1: 1s frozen core for N, C, and O. ADF-2: 1s frozen core for N, C, and O and 1s−3p frozen core for Mn. ORCA and ADF-3: no frozen core. RMS: root-mean-square deviation between theory and experiment for all displayed bond distances; see Figure 1 for numbering. [b] X-ray data of the $[Mn^{III}Mn^{IV}(\mu\text{-}O)_2(\mu\text{-}OAc)DTNE]^{2+}$ complex (counterions: tetraphenylborate).[33]

Considering the Mn−O bond distances of complex **1**, Table 1 shows, in general, very good agreement between the theoretical results for the bs state and the experiment, while somewhat larger deviations up to 0.1 Å were observed for the weaker metal−nitrogen bonds. Nevertheless, the expected Jahn−Teller distortion of the Mn^{III} site with a high spin d^4 configuration is very well reproduced in all calculations.

Note that such a detailed comparison between experimental and calculated geometries requires very accurate X-ray data as could be obtained for the $[Mn^{III}Mn^{IV}(\mu\text{-}O)_2(\mu\text{-}OAc)DTNE](BPh_4)_2$ complex.[33] Many other crystal structures of mixed valence metal complexes suffer from statistical disorder that leads to arithmetically averaged bond distances. This was found, for example, for the methylated derivative of the DTNE complex[33] or the related $[Mn^{III}Mn^{IV}(\mu\text{-}O)_2(\mu\text{-}OAc)(TACN)_2](BPh_4)_2$[73] and for $[Mn^{III}Mn^{IV}(\mu\text{-}O)_2(phen)_4](ClO_4)_3$ species.[74]

4.2. Spin Density Analysis. Mulliken spin densities of the manganese centers of complex **1** are given in Table 2.[75] In general, the calculated values for the high spin and broken symmetry states clearly indicate the trapped character of the mixed valence Mn^{III}/Mn^{IV} complex, in line with the results from

(71) Neese, F. *J. Chem. Phys.* **2003**, *118*, 3939−3948.
(72) Weltner, W., Jr. *Magnetic Atoms and Molecules*; Dover Publications: New York, 1983.
(73) Wieghardt, K.; Bossek, U.; Zsolnai, L.; Huttner, G.; Blondin, G.; Girerd, J. J.; Babonneau, F. *J. Chem. Soc., Chem. Commun.* **1987**, 651−653.
(74) Stebler, M.; Ludi, A.; Burgi, H. B. *Inorg. Chem.* **1986**, *25*, 4743−4750.
(75) Mulliken, R. S. *J. Chem. Phys.* **1962**, *36*, 3428−3439.

Table 2. Manganese Mulliken Spin Densities[a]

	BP ORCA-1	B3LYP ORCA-2	BP ADF-1	BP ADF-2	BP ADF-3
		high spin state			
Mn^{III}	+3.79	+3.86	+3.77	+3.76	+3.77
Mn^{IV}	+2.75	+2.87	+2.71	+2.71	+2.71
		broken symmetry state			
Mn^{III}	+3.47	+3.87	+3.43	+3.46	+3.44
Mn^{IV}	−2.37	−2.73	−2.31	−2.33	−2.32

[a] All values at the level of optimization.

geometry optimization. The obtained Mn spin densities are close to the formal values of four (Mn^{III}) and three (Mn^{IV}) and show the rotation of the spin vector at the Mn^{IV} center between the hs and bs states. The ADF results indicate that there is no influence of the frozen core approximation on the manganese spin densities. Furthermore, these results are in very good agreement with the BP results from ORCA despite the use of very different basis sets (GTOs in ORCA and STOs in ADF). The calculated values compare well with the manganese spin densities of +3.2 and −2.3 obtained from BP calculations on the bs state of the $[Mn^{III}Mn^{IV}(\mu\text{-}O)_2(\mu\text{-}OAc)(TACN)_2]^{2+}$ complex.[38] The B3LYP spin densities from our study turn out to be somewhat larger than the BP values. This is expected from the general tendency of hybrid functionals to give more ionic metal−ligand bonds compared to GGA functionals that tend to overestimate metal−ligand covalencies.[76,77] The origin of this effect may be attributed to a reduced self-interaction error in the hybrid functionals.[78]

4.3. Heisenberg Exchange Coupling Constants. Magnetic susceptibility studies yielded an exchange coupling constant J of $-110\ cm^{-1}$ for complex **1**.[33] The antiferromagnetic coupling indicates that the low spin state is more stable than the high spin state, which is well reproduced by our calculations. J can be calculated either employing the adiabatic energy difference of the hs and bs states (denoted as E_{hs} and E_{bs}) or using the energy difference between the hs state from geometry optimization and the bs state employing the hs state geometry ($E_{bs//hs}$). Theoretically, the former approach is preferred since the experiment clearly is an adiabatic measurement. Calculations at one fixed geometry are necessarily biased in favor of the state for which the geometry optimization has been carried out. In the present case, the changes in the calculated J values are limited though not negligible, which underlines the difficulty of an accurate calculation of the small energetic separations between the different spin states (Table 3). The strong dependence of these energy gaps on the Mn−Mn distance was investigated by Delfs and Stranger in their study on the $[Mn_2(\mu\text{-}O)_3(NH_3)_6]^{2+}$ complex (cf. Figure 3 in their work).[35] Employing the BP functional, we found the typical overestimation of J. In contrast, very accurate results were obtained by the B3LYP hybrid functional.

Very similar exchange coupling constants were obtained employing Yamaguchi's eq 4,[41] which indicates the validity of the weak coupling regime implied by eq 2.

As shown previously, plots of the corresponding orbitals are helpful for a better understanding of the electronic structure in exchange coupled systems.[43,79] Figure 2 shows the corresponding orbitals of the seven magnetic electrons of complex **1** in the bs state. They give rise to three exchange pathways **1**−**3** with reasonable overlap. Pathway **1** is characterized as a crossed σ/π pathway with in-plane oxo p-orbitals. Pathways **2** and **3** can be described as symmetric π/π pathways caused by the interaction between out-of-plane oxo p-orbitals and metal d-orbitals. This indicates that the exchange interaction is mediated by superexchange via the μ-oxo atoms that is in line with the results obtained for other oxo-bridged dinuclear manganese complexes.[35−37,39,42]

Table 3. Calculated Exchange Coupling Constants J/cm^{-1} [a]

	BP ORCA-1	B3LYP ORCA-2	B3LYP//BP ORCA-3	BP ADF-1	BP ADF-2	BP ADF-3
bs//hs; hs[b]	−237	−120	−119	−253	−252	−254
bs; hs[c]	−297	−127	−90	−310	−296	−309

[a] Experimental value of the $[Mn^{III}Mn^{IV}(\mu\text{-}O)_2(\mu\text{-}OAc)DTNE](BPh_4)_2$ complex: $J = -110\ cm^{-1}$.[33] All computed values from eq 2. Basis sets: TZVPP (Mn) and DZP (other elements) for all ORCA calculations; IV (Mn) and III (other elements) for all ADF calculations. ADF-1: 1s frozen core for N, C, and O. ADF-2: 1s frozen core for N, C, and O and 1s−3p frozen core for Mn. ADF-3: no frozen core. [b] E_{bs} from bs single-point calculation on hs state geometry; E_{hs} from geometry optimization. [c] E_{bs} and E_{hs} from geometry optimizations of the respective electronic states.

4.4. The Molecular *g*-Tensor. An almost axially symmetric molecular g-tensor with $g_x \approx g_y$ close to g_e and $g_z = 1.9838$ was found for complex **1** in the experiments. g_x and g_y were oriented along the connecting lines between the μ-oxo atoms O_1 and O_2 and the metal centers, respectively (Figure 1).[33,34] These properties were well-reproduced in our calculations: Similar g-tensor orientations could be obtained, and the characteristic shift of the g_z component was also obtained, while g-values close to g_e were calculated for g_x and g_y (Table 4). Better agreement between theory and experiment was found for the B3LYP calculations. The underlying g-tensor site values using eqs 15 and 16 turned out to be physically meaningful. This is additional support for our simple model for the extraction of g-tensor site values from the calculations on the hs and bs states. At the B3LYP level of theory, values of $g_x = 2.001$, $g_y = 2.000$, and $g_z = 1.992$ were calculated for the Mn^{III} site. These numbers compare very well with $g_\perp = 2.00$ and $g_\parallel = 1.99$ obtained for Mn^{III} in TiO_2.[80] Furthermore, three negative g-shifts are also expected from ligand field theory for transition metals with high spin d^4 configuration.[81] The calculated g-tensor site values for Mn^{IV} were $g_x = 1.998$, $g_y = 1.999$, and $g_z = 2.001$ (B3LYP). Again, three negative g-shifts were in accordance with ligand field theory and experiments.[81,82]

4.5. Manganese Hyperfine Tensors. Experimental ^{55}Mn hyperfine data are available from simultaneous fits of EPR spectra taken at X- (9 GHz), Q- (34 GHz), and W-band (94 GHz) frequencies.[33,34] These values are given in Table 5 and are compared with our computed manganese site values a_{iso}(site) and the spin-projected isotropic and anisotropic hfc's A_{iso} and A'.

The calculations nicely reproduce the main qualitative features of the experimental ^{55}Mn hyperfine tensors: (i) Correct signs

(76) Szilagyi, R. K.; Metz, M.; Solomon, E. I. *J. Phys. Chem. A* **2002**, *106*, 2994−3007.
(77) Neese, F. *J. Phys. Chem. A* **2001**, *105*, 4290−4299.
(78) Patchkovskii, S.; Autschbach, J.; Ziegler, T. *J. Chem. Phys.* **2001**, *115*, 26−42.
(79) Herebian, D.; Wieghardt, K. E.; Neese, F. *J. Am. Chem. Soc.* **2003**, *125*, 10997−11005.
(80) Gerritsen, H. J.; Sabisky, E. S. *Phys. Rev.* **1963**, *132*, 1507.
(81) Neese, F.; Solomon, E. I. In *Magnetism: Molecules to Materials*; Miller, J. S., Drillon, M., Eds.; Wiley VCH: Weinheim, Germany, 2003; pp 345−466.
(82) From, W. H.; Dorain, P. B.; Kikuchi, C. *Phys. Rev. A* **1964**, *135*, A710.

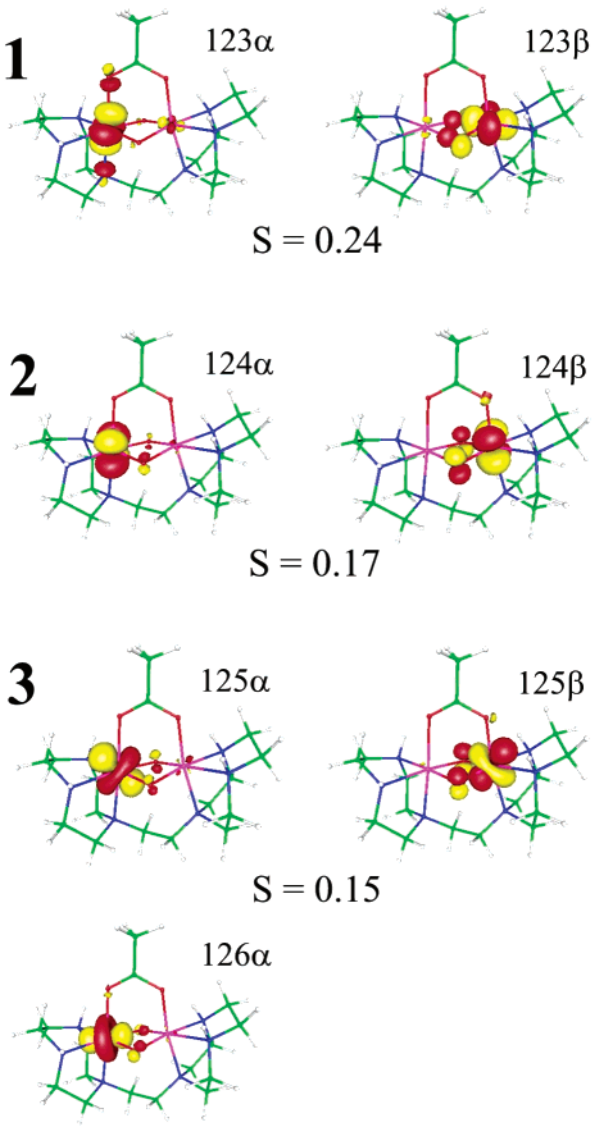

Figure 2. The corresponding magnetic orbitals from the B3LYP calculation (bs state), labeled by the number of the molecular orbitals (MO) in every spin representation. The interaction of the four magnetic (unpaired) Mn^{III} α-electrons with the three magnetic Mn^{IV} β-electrons gives reasonable overlap for three superexchange pathways **1**−**3**, e.g., pathway **1** is caused by an interaction of MO 123α with MO 123β. *S* denotes the calculated overlap values for pathways **1**−**3**.

Table 4. Calculated *g*-Tensors from Coupled Perturbed Kohn−Sham Theory (ORCA)[a]

	BP//BP	B3LYP//B3LYP	B3LYP//BP	exptl[b]
g_x	1.992	2.003	2.002	2.0013
g_y	1.996	2.001	2.002	1.9974
g_z	1.981	1.983	1.982	1.9838
g_{iso}	1.989	1.996	1.995	1.9942

[a] Basis sets for single-point calculations: CP(PPP) (Mn) and EPR-II (other elements). [b] Data for the $[Mn^{III}Mn^{IV}(\mu\text{-O})_2(\mu\text{-OAc})DTNE](BPh_4)_2$ complex.[34]

of the isotropic hfc's were obtained in all cases for both metals except for the ADF-2 calculation with an unreasonable large 1s−3p manganese frozen core (data not shown). (ii) The computed Mn^{III} isotropic hfc's were about twice as large as those of Mn^{IV}, and both manganese ions showed similar intrinsic site values. (iii) Rhombic dipolar hyperfine tensors were obtained for both metals. (iv) The strongest anisotropy was observed for the Mn^{III} site. (v) An almost collinear axis system for the *g*-tensor and the hyperfine tensors was found (typical deviations of ∼10°).

Table 5. ^{55}Mn Hyperfine Data (MHz): Site Values a_{iso}(Site) and Spin-Projected Isotropic and Anisotropic hfc's A_{iso} and A'[a]

		BP//BP ORCA-1	B3LYP//B3LYP ORCA-2	B3LYP//BP ORCA-3	BP//BP ADF-1	BP//BP ADF-3	exptl[b]
Mn^{III}	a_{iso}(site)	−129 (−123)	−134 (−128)	−137 (−131)	−82	−82	−195
	A_{iso}	−258 (−246)	−267 (−255)	−275 (−263)	−164	−164	−389
	A'_x	−57 (−59)	−55 (−59)	−58 (−63)	−61	−61	−17
	A'_y	−29 (−31)	−52 (−56)	−50 (−54)	−25	−25	−81
	A'_z	+86 (+90)	+106 (+115)	+109 (+117)	+85	+86	+92
Mn^{IV}	a_{iso}(site)	−124 (−119)	−142 (−131)	−139 (−129)	−84	−84	−207
	A_{iso}	+124 (+119)	+142 (+131)	+139 (+129)	+84	+84	+207
	A'_x	−8 (−8)	−3 (−1)	−4 (−4)	−8	−8	+14
	A'_y	+31 (+28)	+8 (+7)	+11 (+10)	+26	+26	−14
	A'_z	−24 (−20)	−5 (−5)	−7 (−6)	−18	−18	+6

[a] In Parenthesis: Results from ORCA without Spin−Orbit Contributions. Basis sets for single-point calculations: CP(PPP) (Mn) and EPR-II (other elements) for all ORCA calculations; IV (Mn) and III (other elements) for all ADF calculations. ORCA-1, ORCA-2, ORCA-3, and ADF-3: no frozen core. ADF-1: 1s frozen core for N, C, and O. For coordinate system, see Figure 1. [b] Experimental data of the $[Mn^{III}Mn^{IV}(\mu\text{-O})_2(\mu\text{-OAc})DTNE](BPh_4)_2$ complex.[34]

Despite this qualitative agreement, rather different manganese hyperfine data were obtained by ADF and ORCA. This is only to a minor extent due to the inclusion of the orbital hyperfine part in the ORCA calculations (Table 5). It is therefore likely that the rather large (17s11p5d1f) → [17s7p3d1f] manganese Gaussian-type basis set used in ORCA is responsible for the better isotropic hfc's obtained with this program in comparison with the ADF results.

From the work of Munzarová and Kaupp, the deviation between the calculated and measured ^{55}Mn isotropic hfc's is expected.[83] These authors attribute the underestimation of the experimental isotropic values to the inadequate description of spin polarization by present day density functional methods. In the present case, the calculated values are too small in comparison with the experimental values by a factor

$$f = \frac{A_{iso}(\text{exptl})}{A_{iso}(\text{calcd})} \qquad (21)$$

of 1.4−1.7 (ORCA) and 2.4−2.5 (ADF). Somewhat surprising, very similar isotropic hfc's were obtained with the two density functionals BP and B3LYP in the ORCA calculations. Regarding the anisotropic hfc's, very similar results were obtained with ORCA and ADF at the BP level, which indicates the expected weaker basis set dependence than in the case of the isotropic hfc's.

The underestimation of the isotropic ^{55}Mn hfc's appears to be a general problem of such DFT studies and is also observed in calculations on comparable mononuclear manganese complexes. Considering the $[Mn(H_2O)_6]^{2+}$ complex as a typical example, an experimental hfc $A_{iso} = -264$ MHz was found.[84] In contrast, isotropic hfc's of −163 MHz (B3LYP//BP, ORCA) and −120 MHz (BP//BP, ADF) were calculated in this work employing the same basis sets (see Tables 5 and 6) as for the dinuclear manganese complex. From eq 21, factors *f* of 1.6 (ORCA) and 2.2 (ADF) were calculated, similar to those

(83) Munzarová, M.; Kaupp, M. *J. Phys. Chem. A* **1999**, *103*, 9966−9983.
(84) Luckhurst, G. R.; Pedulli, G. F. *Mol. Phys.* **1971**, *22*, 931−935.

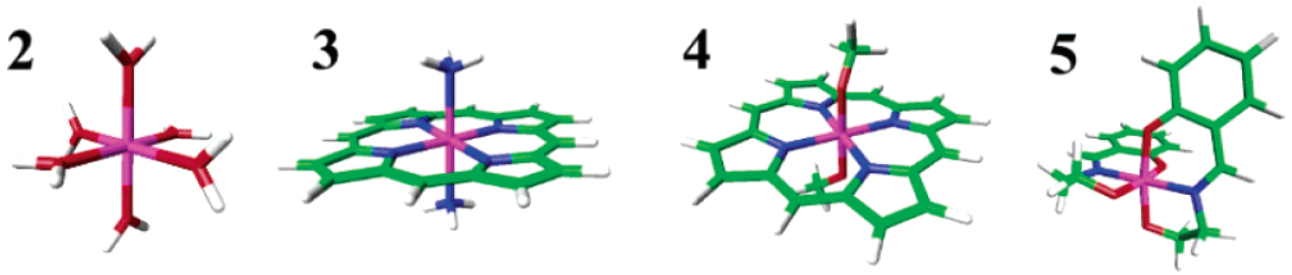

Figure 3. Geometry-optimized structures (using BP functional, TZVPP (Mn), and DZP (other elements) basis sets; ORCA) of the mononuclear manganese complexes $[Mn^{II}(H_2O)_6]^{2+}$ (**2**), $[Mn^{II}(Porph)(NH_3)_2]$ (**3**), $[Mn^{IV}(Porph)(OCH_3)_2]$ (**4**), and $[Mn^{IV}(SALAHE)_2]$ (**5**). Porph = porphinate, $H_2SALAHE$ = 1-hydroxy-2-methyl-2-(salicylideneamino)ethane.

Table 6. Theoretical Isotropic ^{55}Mn hfc's (B3LYP//BP, ORCA) of Mononuclear Manganese Complexes (see Figure 3)[a]

		A_{iso} (calcd)	A_{iso}^{est} (exptl)	$f(A_{iso})$
	mononuclear complexes			
Mn^{II}	$[Mn(H_2O)_6]^{2+}$	−165	−264[b]	1.6
	$[Mn(Porph)(NH_3)_2]$	−115	−204[c]	1.8
Mn^{IV}	$[Mn(Porph)(OCH_3)_2]$	−133	−202[d]	1.5
	$[Mn(SALAHE)_2]$	−128	−216[e]	1.7
	dinuclear complexes			
Mn^{III}	$[Mn^{III}Mn^{IV}(\mu\text{-}O)_2(\mu\text{-}OAc)DTNE]^{2+}$	−267	−389[f]	1.5
Mn^{IV}	$[Mn^{III}Mn^{IV}(\mu\text{-}O)_2(\mu\text{-}OAc)DTNE]^{2+}$	+142	+207[f]	1.5

[a] Estimated ratio f between experimental and calculated ^{55}Mn isotropic hfc's in comparison with the BS-DFT results for the $[Mn^{III}Mn^{IV}(\mu\text{-}O)_2(\mu\text{-}OAc)DTNE]^{2+}$ complex. Results from B3LYP single-point calculations with basis sets CP(PPP) (Mn) and EPR-II (other elements) on geometry-optimized structures from BP calculations employing the TZVPP (Mn) and DZP (other elements) basis sets. [b] Experimental hyperfine data from studies performed on $[Mn^{II}(H_2O)_6]^{2+}$.[84] [c] Experimental hyperfine data from studies performed on $[Mn^{II}TPP]$.[85] [d] Experimental hyperfine data from studies performed on $[Mn^{IV}TPP(OCH_3)_2]$.[85,87] [e] Experimental hyperfine data from studies performed on $[Mn^{IV}(SALAHE)_2]$.[86] [f] Experimental hyperfine data from studies performed on $[Mn^{III}Mn^{IV}(\mu\text{-}O)_2(\mu\text{-}OAc)DTNE](BPh_4)_2$.[34] TPP = tetraphenylporphinate.

obtained for the manganese atoms in the dinuclear DTNE complex **1** (ORCA: 1.4−1.7, ADF: 2.4−2.5). Other experimental hyperfine data are available for $[Mn^{II}TPP]$,[85] $[Mn^{IV}(TPP)(OMe)_2]$, and $[Mn^{IV}(SALAHE)_2]$.[86] Calculations on these systems were performed employing the model systems **2**−**5** displayed in Figure 3 (B3LYP//BP, ORCA). Also for these complexes, similar ratios f between theoretical and experimental isotropic ^{55}Mn hfc's were obtained (Table 6). This indicates that the underestimation of the isotropic ^{55}Mn hfc's in complex **1** is not basically anchored in the broken symmetry and spin projection formalisms. A systematic deviation allows, however, the use of scaling factors for the estimation of experimental data, and we propose the use of the value 1.5 for future studies on such dinuclear manganese systems employing the same level of theory.

4.6. Manganese Nuclear Quadrupole Tensors. The almost octahedral environment of both metal ions of complex **1** is expected to result in rather small nuclear quadrupole tensors. This is confirmed by the calculations. Independent of the chosen method or program, no eigenvalue of the ^{55}Mn nuclear quadrupole tensors larger than 4 MHz was obtained in this work (Table 7). Considering the experimental data, a quadrupole splitting could not be detected in the pulse ^{55}Mn ENDOR spectra of complex **1** due to line widths of about 8 MHz.[88] Nevertheless,

Table 7. Calculated ^{55}Mn Nuclear Quadrupole Tensor Components P of $[Mn^{III}Mn^{IV}(\mu\text{-}O)_2(\mu\text{-}OAc)DTNE]^{2+}$ (MHz), in Comparison with Experimental Data of Related $Mn^{III}Mn^{IV}$ Systems[a]

		BP//BP ORCA-1	B3LYP//B3LYP ORCA-2	B3LYP//BP ORCA-3	BP//BP ADF-1	BP//BP ADF-3	exptl MDTNE[b]	exptl BIPY[c]
Mn^{III}	P_x	+1.7	+2.3	+2.3	+1.8	+1.9	−0.3	+1.5 (+1.65)
	P_y	−0.2	+0.4	+0.6	−0.3	−0.3	+1.35	+0.9 (+1.35)
	P_z	−1.4	−2.7	−2.9	−1.5	−1.1	−1.05	−2.4 (−3.0)
Mn^{IV}	P_x	−1.6	−1.3	−1.4	−1.4	−1.4	−1.2	−1.0 (−0.5)
	P_y	−2.1	−1.8	−1.7	−2.2	−2.1	−1.1	−0.5 (−0.9)
	P_z	+3.8	+3.1	+3.1	+3.5	+3.5	+2.3	+1.5 (+1.4)

[a] Basis sets for single-point calculations: CP(PPP) (Mn) and EPR-II (other elements) for all ORCA calculations; IV (Mn) and III (other elements) for all ADF calculations. ORCA and ADF-3: no frozen core. ADF-1: 1s frozen core for N, C, and O. [b] Experimental data for the $[Mn^{III}Mn^{IV}(\mu\text{-}O)_2(\mu\text{-}OAc)(CH_3)_4DTNE](BPh)_4$ complex.[88] [c] Experimental data for the $[Mn^{III}Mn^{IV}(\mu\text{-}O)_2BIPY_4](ClO_4)_3$ complex from Schäfer[88] and Randall et al. in parentheses.[89]

experimental nuclear quadrupole data are available for the closely related complex $[Mn^{III}Mn^{IV}(\mu\text{-}O)_2(\mu\text{-}OAc)(CH_3)_4DTNE]^{2+}$ and other dinuclear manganese systems (see Table 7).[88,89] The tensor components P_z (see Figure 1 for the molecular axes system) have negative signs for Mn^{III} and positive signs for Mn^{IV}, both in the calculations and experiments. This is in line with the model of a prolate electric field gradient along the z-axis for the Jahn−Teller distorted Mn^{III} site and an oblate electric field gradient on Mn^{IV} and consistent with basic ligand field arguments.[89] These different electronic distributions around the metals are clearly displayed in the geometries: considering the Mn^{III} site, the "axial" Mn_1-O_4 bond is longer than the "in plane" Mn_1-N_2 and Mn_1-N_3 bonds, while at the Mn^{IV} site, the Mn_2-O_3 bond is shorter than the corresponding Mn_2-N_5 and Mn_2-N_6 bonds (see Figure 1 and Table 1).

4.7. Nitrogen Hyperfine Tensors and Nuclear Quadrupole Coupling Constants. Only one large, almost isotropic ^{14}N hfc of ∼10 MHz was found in the cw-ENDOR experiments of complex **1**.[33] The signal was assigned to the nitrogen atom N_1, which is axially bound to the Mn^{III} center (Figure 1). This assignment is corroborated by our calculations, which show one dominant isotropic hyperfine coupling constant A_{iso} = 8−12 MHz for this nitrogen nucleus (Table 8). Nevertheless, the calculations gave significant dipolar hyperfine contribution in contrast to the almost isotropic experimental signal. In view of previous studies on ^{14}N hfc's in Cu^{II} complexes it is likely,

(85) Perrée-Fauvet, M.; Gaudemer, A.; Bonvoisin, J.; Girerd, J. J.; Boucly-Goester, C.; Boucly, P. *Inorg. Chem.* **1989**, *28*, 3533−3538.
(86) Kessissoglou, D. P.; Li, X. H.; Butler, W. M.; Pecoraro, V. L. *Inorg. Chem.* **1987**, *26*, 2487−2492.
(87) Camenzind, M. J.; Hollander, F. J.; Hill, C. L. *Inorg. Chem.* **1983**, *22*, 3776−3784.
(88) Schäfer, K. O. *Exchange Coupled Manganese Complexes: Model Systems for the Active Centres of Redoxproteins Investigated with EPR Techniques.* Dissertation, Technische Universität Berlin, Germany, 2002.
(89) Randall, D. W.; Sturgeon, B. E.; Ball, J. A.; Lorigan, G. A.; Chan, M. K.; Klein, M. P.; Armstrong, W. H.; Britt, R. D. *J. Am. Chem. Soc.* **1995**, *117*, 11780−11789.

Table 8. Spin-Projected ^{14}N Hyperfine Data and Nuclear Quadrupole Coupling Constants (MHz)[a]

			BP//BP ORCA-1	B3LYP//B3LYP ORCA-2	B3LYP//BP ORCA-3	BP//BP ADF-1	BP//BP ADF-3
site 1	N_1	A_{iso}	+8.4	+12.0	+12.6	+11.1	+8.7
		A'_1	−1.8	−2.4	−2.3	−1.8	−1.8
		A'_2	−1.6	−2.2	−2.2	−1.6	−1.6
		A'_3	+3.4	+4.6	+4.5	+2.3	+3.4
		$\|\chi\|$	2.1	2.4	2.4	1.9	1.9
	N_2	A_{iso}	−1.5	−2.1	−1.5	−2.8	−1.1
		$\|\chi\|$	1.7	1.8	1.8	1.5	1.5
	N_3	A_{iso}	−1.1	−1.8	−1.1	−1.3	−0.9
		$\|\chi\|$	1.7	1.8	1.8	1.5	1.5
site 2	N_4	A_{iso}	+2.4	+1.9	+2.3	+1.6	+1.1
		$\|\chi\|$	1.6	1.6	1.6	1.4	1.4
	N_5	A_{iso}	+3.0	+1.6	+1.7	+2.3	+1.7
		$\|\chi\|$	1.7	1.7	1.7	1.5	1.5
	N_6	A_{iso}	+2.8	+1.3	+1.6	+2.3	+1.6
		$\|\chi\|$	1.7	1.7	1.7	1.4	1.4

[a] Basis sets for single-point calculations: CP(PPP) (Mn) and EPR-II (other elements) for all ORCA calculations; IV (Mn) and III (other elements) for all ADF calculations. ORCA and ADF-3: no frozen core. ADF-1: 1s frozen core for N, C, and O. Very similar results were obtained with an additional Mn 1s−3p frozen core (ADF-2, results not shown). Experimental values of the $[Mn^{III}Mn^{IV}(\mu\text{-}O)_2(\mu\text{-}OAc)(CH_3)_4DTNE](BPh)_4$ complex: $A = 9.8$ MHz and $\chi = 2.20$ MHz, assigned to N_1.[33]

however, that the hyperfine anisotropy of this metal bound nitrogen atom is also overestimated in our calculations.[77,90]

Much smaller isotropic hfc's have been calculated for all other nitrogen nuclei, and experimental hyperfine data for these nuclei in complex **1** are not available. However, a further ^{14}N hfc of 2.9 MHz could be obtained, e.g., for the $[Mn^{III}Mn^{IV}(\mu\text{-}O)_2(\mu\text{-}OAc)(TACN)_2](ClO_4)_3$ complex from ESEEM spectroscopy, and was assigned to the equatorial nitrogens at the Mn^{III} site.[33]

Table 8 also includes ^{14}N nuclear quadrupole coupling constants. The largest values for $|\chi|$ were obtained for N_1 (1.9−2.4 MHz), in very good agreement with the experimental value of 2.20 MHz.[33]

4.8. Hydrogen Hyperfine Tensors. In the experimental study, significant ^1H hyperfine interactions were only found for those hydrogen atoms directly attached to the nitrogen nuclei of complex **1** (Figure 1).[33] Furthermore, the hydrogen atoms at N_2/N_3 and, likewise, at N_5/N_6 are exposed to rather similar chemical environments. In consequence, only one ^1H hyperfine tensor could be measured for each site (Table 9). The calculations are in agreement with these findings and show similar hyperfine data for both pairs of hydrogen atoms. In general, good agreement between theory and experiment has been found. Similar results were obtained with the BP and B3LYP density functionals.

Through application of the extended point-dipole model, the location of hydrogen atoms in dinuclear exchange coupled metal clusters can be estimated from measured anisotropic ^1H hyperfine data A'.[91] In the opposite way, the ^1H hyperfine data can be obtained from the distances r_A, r_B, and the angle Θ between the hydrogen nucleus and the spin centers (Figure 4). Making use of the spin projection coefficients of $c_1 = 2$ for Mn^{III} and $c_2 = -1$ for Mn^{IV} one obtains:

$$A' = c\cdot\mathrm{diag}(-\delta, -\Gamma + \delta/2, \Gamma + \delta/2) \qquad (22)$$

Table 9. Spin-Projected ^1H Hyperfine Coupling Constants (MHz)[a]

	BP//BP ORCA-1	B3LYP//B3LYP ORCA-2	B3LYP//BP ORCA-3	BP//BP ADF-1	BP//BP ADF-3	exptl[b]
			H−N_3, site 1			
A_{iso}	+4.9	+4.9	+4.6	+5.1	+5.1	+3.1
A'_1	−7.1	−8.1	−7.8	−7.2	−7.2	−8.7
A'_2	−5.8	−6.5	−6.4	−5.9	−5.9	−8.0
A'_3	+12.9	+14.6	+14.2	+13.1	+13.1	+16.7
			H−N_2, site 1			
A_{iso}	+5.3	+5.3	+4.9	+5.8	+5.8	+3.1
A'_1	−7.0	−8.0	−7.8	−6.9	−6.9	−8.7
A'_2	−5.7	−6.3	−6.2	−5.8	−5.8	−8.0
A'_3	+12.7	+14.3	+14.0	+12.6	+12.6	+16.7
			H−N_6, site 2			
A_{iso}	−2.4	−2.7	−2.9	−2.4	−2.4	−1.5
A'_1	−5.8	−6.9	−6.8	−5.6	−5.6	−7.2
A'_2	+2.2	+2.9	+2.7	+2.2	+2.1	+2.8
A'_3	+3.5	+4.1	+4.1	+3.4	+3.4	+4.4
			H−N_5, site 2			
A_{iso}	−2.8	−3.0	−3.2	−3.0	−3.0	−1.5
A'_1	−5.7	−6.8	−6.7	−5.6	−5.6	−7.2
A'_2	+2.3	+2.9	+2.8	+2.2	+2.2	+2.8
A'_3	+3.4	+3.9	+3.9	+3.3	+3.3	+4.4

[a] Basis sets for single-point calculations: CP(PPP) (Mn) and EPR-II (other elements) for all ORCA calculations; IV (Mn) and III (other elements) for all ADF calculations. ORCA and ADF-3: no frozen core. ADF-1: 1s frozen core for N, C, and O. Very similar results were obtained with an additional Mn 1s−3p frozen core (ADF-2, results not shown). [b] Experimental data of the $[Mn^{III}Mn^{IV}(\mu\text{-}O)_2(\mu\text{-}OAc)(CH_3)_4DTNE](BPh)_4$ complex.[33] Similar hfc's were obtained for the hydrogen atoms attached to N_2/N_3 and to N_5/N_6, respectively.

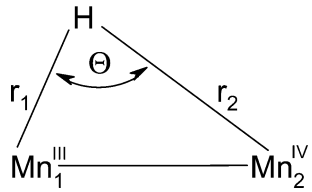

Figure 4. Geometrical parameters used in the extended point-dipole model for the estimation of ^1H anisotropic hfc's.

with

$$\delta = 2\cdot r_1^{-3} - r_2^{-3} \qquad (23)$$

$$\Gamma = \frac{3}{2}\sqrt{4r_1^{-6} - 4r_1^{-3}r_2^{-3}\cos(2\cdot\Theta) + r_2^{-6}} \qquad (24)$$

where $c = g_e\beta_e g_N\beta_N/h = 79.2\ MHz$ Å^3 for protons. g_e and g_N are the electron and nuclear g-values, β_e and β_N are the electron and nuclear Bohr magnetons, and h is Planck's constant.

Due to the frequent use of the extended point-dipole model for predicting geometrical details from EPR/ENDOR parameters, e.g., for dinuclear manganese complexes,[33,91,92] it was interesting to check the quality of this approximation in application to complex **1**. Therefore, ^1H hfc's were estimated from this model employing the geometrical parameters r_A, r_B, and Θ from the available X-ray structure[33] and from the DFT geometry optimizations performed in this work. From Table 10 it is evident that the hyperfine data from the extended point-dipole model are very close to the experimental ^1H hyperfine values, underlining the validity of the model for the manganese complex under investigation. Furthermore, the ^1H hyperfine data from the extended point-dipole model compare better with the experimental data than the hfc's directly obtained in the DFT

(90) Jaszewski, A. R.; Jezierska, J. *Chem. Phys. Lett.* **2001**, *343*, 571−580.
(91) Zweygart, W. *ESR und ENDOR−Untersuchungen an mehrkernigen gemischtvalenten Mangankomplexen als Modelle für das wasserstoffoxidierende Enzymsystem im Photosystem II*. Dissertation, Technische Universität Berlin, Germany, 1995.
(92) Randall, D. W.; Gelasco, A.; Caudle, M. T.; Pecoraro, V. L.; Britt, R. D. *J. Am. Chem. Soc.* **1997**, *119*, 4481−4491.

Table 10. Comparison of ^{1}H Hyperfine Data (MHz) for the Proton Attached to N_3 (Figure 1) Obtained from Experiments, Extended Point-Dipole Model, and DFT Calculations

	exptl[a]	extended point-dipole model on exptl structure[b]	extended point-dipole model on calcd structure[c]	DFT calcd B3LYP//B3LYP ORCA-2[d]
A'_1	−8.7	−9	−8.3	−8.1
A'_2	−8.0	−8	−8.2	−6.5
A'_3	+16.7	+17	+16.5	+14.6

[a] Measured data of the $[Mn^{III}Mn^{IV}(\mu\text{-}O)_2(\mu\text{-}OAc)(CH_3)_4DTNE](BPh)_4$ complex.[33] [b] hfc's from the extended point-dipole model employing the X-ray data of $[Mn^{III}Mn^{IV}(\mu\text{-}O)_2(\mu\text{-}OAc)(CH_3)_4DTNE](BPh)_4$, but with modeled N−H bond lengths (values from Schäfer et al.).[33] [c] hfc's from the extended point-dipole model employing geometrical parameters from the B3LYP geometry-optimized structure (ORCA-2). [d] Calculated DFT results (ORCA-2).

calculations. This is somewhat surprising since the point-dipole model makes use of idealized spin densities (only) at the manganese centers, while the spin density distributions from the DFT calculations should be closer to reality.

5. Summary and Conclusions

The electronic structure of the $[Mn^{III}Mn^{IV}(\mu\text{-}O)_2(\mu\text{-}OAc)\text{-}DTNE]^{2+}$ complex was investigated by density functional theory employing the broken symmetry approach and spin projection. Geometry optimization of the complex yielded distinctly different Mn^{III} and Mn^{IV} sites for the high spin and broken symmetry states. This trapped valence character is in agreement with the experimental results. A comparison of the geometrical parameters from theory with the X-ray structure shows good agreement. Somewhat smaller deviations between theory and experiment were obtained for the broken symmetry state in comparison to the high spin state geometry. The BP functional yielded more accurate geometrical parameters than the B3LYP method. In the next step, the Heisenberg exchange coupling constant J of the $[Mn^{III}Mn^{IV}(\mu\text{-}O)_2(\mu\text{-}OAc)DTNE]^{2+}$ complex was calculated. Employing the BP functional, the typical overestimation of J by factors between 2 and 3 was found. In contrast, very good agreement between theory and experiment could be obtained with the B3LYP hybrid density functional. The frozen core approximation was only of minor influence on geometries, spin densities, and exchange coupling constants.

Spin projection was used for the estimation of hyperfine parameters and the g-tensor of the antiferromagnetic state, while the nuclear quadrupole coupling constants were calculated from electric field gradients without spin projection. The ^{55}Mn hyperfine coupling constants were qualitatively well reproduced. However, large and flexible core basis sets are required for this purpose. The isotropic ^{55}Mn hfc's are distinctly underestimated, but it was shown that similar deviations between theory and experiment occur for DFT calculations on mononuclear manganese complexes, which makes the use of a universal scaling factor of ∼1.5 plausible. The calculated ^{14}N and ^{1}H hyperfine data showed good agreement with the experimental data.

Calculated hyperfine data, nuclear quadrupole tensors, and the g-tensor are reported for the first time for such a magnetically coupled dinuclear manganese complex and overall compare well with the experimental data. The quality of the calculated data shows the potential of the BS-DFT approach for the calculation of EPR parameters in combination with spin projection or mapping procedures. Such calculations will be valuable for a deeper understanding of the electronic structure of magnetically coupled metal systems in general and to evaluate structural proposals from spectroscopic studies. The $Mn_2(\mu\text{-}O)_2(\mu\text{-}OAc)$ structural motif of the investigated cluster is similar to the active center of the manganese catalase. Two X-ray structures are available for the $Mn^{III}Mn^{III}$ states of the enzymes from *Lactobacillus plantarum* and *Thermus thermophilus*.[93,94] The superoxidized $Mn^{III}Mn^{IV}$ state of the manganese catalase is experimentally well characterized and shows data rather similar to those of the DTNE complex investigated here.[31,34,95,96] In consequence, the use of BS-DFT to evaluate the plausibility of possible structures for this system appears to be promising and will be addressed in detail in a forthcoming publication. Furthermore, we plan to extend this work to the lower oxidation states of the manganese catalase active site that are directly relevant for the proposed catalytic cycle of this enzyme.[94] However, these calculations will require an adequate treatment of the zero-field splitting interaction, the theory of which is currently under development in our laboratory.

The elucidation of geometric and electronic structures of oligomeric transition-metal active sites on the basis of a comparison between calculated and measured spectroscopic data is a fairly challenging task and requires the capability to calculate as many observables as possible with an adequate accuracy. We hope that this study, which is focused on geometries, exchange coupling constants, g-tensors, and metal and ligand hyperfine as well as nuclear quadrupole couplings, will prove to be a useful basis for further studies on such systems.

Acknowledgment. Tiqing Liu (Scripps Institute, La Jolla, CA) is acknowledged for his help and for providing the HYPER2000 program. We thank K.-O. Schäfer (TU Berlin, Germany) and D. Case (Scripps) for stimulating discussions. This work has been supported by the priority programs "Molecular Magnetism" (F.N.) and "High-Field EPR in Biology, Chemistry and Physics" (W.L.) of the DFG.

Supporting Information Available: Cartesian coordinates of the $[Mn^{III}Mn^{IV}(\mu\text{-}O)_2(\mu\text{-}OAc)DTNE]^{2+}$ complex from geometry optimization (text and PDF), charges, and net spin densities of the bs state, Heisenberg exchange coupling constants according to Yamaguchi's equation, g-tensor site values, alternative approach for the calculation of g-tensor site values and g-tensors, ^{55}Mn hyperfine coupling constants, and nuclear quadrupole tensors from Hyper2000 (PDF). This material is available free of charge via the Internet at http://pubs.acs.org.

JA0390202

(93) Antonyuk, S. V.; Melik-Adamyan, V. R.; Popov, A. N.; Lamzin, V. S.; Hempstead, P. D.; Harrison, P. M.; Artymyuk, P. J.; Barynin, V. V. *Crystallogr. Rep.* **2000**, *45*, 105−116.
(94) Barynin, V. V.; Whittaker, M. M.; Antonyuk, S. V.; Lamzin, V. S.; Harrison, P. M.; Artymiuk, P. J.; Whittaker, J. W. *Structure* **2001**, *9*, 725−738.
(95) Waldo, G. S.; Yu, S.; Penner-Hahn, J. E. *J. Am. Chem. Soc.* **1992**, *114*, 5869−5870.
(96) Michaud-Soret, I.; Jacquamet, L.; Debaecker-Petit, N.; Le Pape, L.; Barynin, V. V.; Latour, J. M. *Inorg. Chem.* **1998**, *37*, 3874−3876.